Formation of Nocturnal Offshore Rainfall near the West Coast of Sumatra: Land Breeze or Gravity Wave?

HEDANQIU BAI,[a] GUMILANG DERANADYAN,[b] COURTNEY SCHUMACHER,[a] AARON FUNK,[a] CRAIG EPIFANIO,[a]
ABDULLAH ALI,[b] ENDARWIN,[b] FACHRI RADJAB,[b] RIRIS ADRIYANTO,[b] NOER NURHAYATI,[b]
YUDHA NUGRAHA,[b] AND ANNISA FAUZIAH[b]

[a] *Department of Atmospheric Sciences, Texas A&M University, College Station, Texas*
[b] *Meteorological, Climatological, and Geophysical Agency, Jakarta, Indonesia*

ABSTRACT: Afternoon deep convection over the Maritime Continent islands propagates offshore in the evening to early morning hours, leading to a nocturnal rainfall maximum over the nearby ocean. This work investigates the formation of the seaward precipitation migration off western Sumatra and its intraseasonal and seasonal characteristics using BMKG C-band radar observations from Padang and ERA5 reanalysis. A total of 117 nocturnal offshore rainfall events were identified in 2018, with an average propagation speed of $4.5 \, \text{m s}^{-1}$ within 180 km of Sumatra. Most offshore propagation events occur when the Madden–Julian oscillation (MJO) is either weak (real-time multivariate MJO index < 1) or active over the Indian Ocean (phases 1–3), whereas very few occur when the MJO is active over the Maritime Continent and western Pacific Ocean (phases 4–6). The occurrence of offshore rainfall events also varies on the basis of the seasonal evolution of the large-scale circulation associated with the Asian–Australian monsoons, with fewer events during the monsoon seasons of December–February and June–August and more during the transition seasons of March–May and September–November. Low-level convergence, resulting from the interaction of the land breeze and background low-level westerlies, is found to be the primary driver for producing offshore convective rain propagation from the west coast of Sumatra. Stratiform rain propagation speeds are further increased by upper-level easterlies, which explains the faster migration speed of high reflective clouds observed by satellite. However, temperature anomalies associated with daytime convective latent heating over Sumatra indicate that gravity waves may also modulate the offshore environment to be conducive to seaward convection migration.

KEYWORDS: Gravity waves; Diurnal effects; Rainfall; Sea breezes; Radars/radar observations

1. Introduction

The complex geography of the so-called Maritime Continent (MC) leads to a strong diurnal cycle in convection and rainfall over land and the coastal ocean. While convection maximizes over land during the day, the afternoon deep convection propagates offshore in the evening to early morning, leading to a nocturnal rainfall maximum over the nearby ocean up to many hundreds of kilometers offshore (e.g., Yang and Slingo 2001; Kikuchi and Wang 2008; Biasutti et al. 2012). Numerous factors can affect the diurnal cycle of convection over land during the day and the offshore propagation of rainfall at night including the size, orientation, curvature, and topography of the islands (e.g., Gray and Jacobson 1977; Sobel et al. 2011; Biasutti et al. 2012), the direction and speed of the background flow (e.g., Houze et al. 1981; Wang and Sobel 2017; Du and Rotunno 2018), and the passage of the Madden–Julian oscillation (MJO; Madden and Julian 1972) and convectively coupled equatorial waves (e.g., Tian et al. 2006; Rauniyar and Walsh 2011; Peatman et al. 2014; Birch et al. 2016; Zhang and Ling 2017). Both observations and models have been used to describe the resulting speed of and possible mechanisms causing the nocturnal offshore rainfall migration.

Nocturnal rainfall maxima that migrate from land to coastal ocean have been found to have speeds ranging from 3 to $20 \, \text{m s}^{-1}$ across the global tropics. Yang and Slingo (2001) estimated offshore propagation speeds of $15–20 \, \text{m s}^{-1}$ in June–August (JJA) and $10 \, \text{m s}^{-1}$ in December–February (DJF) in the Bay of Bengal using global satellite cloud imagery from the Cloud Archive User Service (CLAUS) dataset. Warner et al. (2003) simulated the westward-propagating speed off the northwest coast of South America as $12 \, \text{m s}^{-1}$ using the fifth-generation Pennsylvania State University–NCAR Mesoscale Model (MM5). Using Climate Prediction Center morphing technique (CMORPH) precipitation, Li and Carbone (2015) estimated the offshore speed to be $10 \, \text{m s}^{-1}$ in both the Bay of Bengal and off the west coast of Colombia. Using the Weather Research and Forecasting (WRF) Model, Vincent and Lane (2016) and Hassim et al. (2016) found offshore speeds of $3–5 \, \text{m s}^{-1}$ from the northeast coast of New Guinea.

Near the west coast of Sumatra, observations and models show speeds of nocturnal offshore rainfall propagation ranging from 3 to $10 \, \text{m s}^{-1}$. Using Tropical Rainfall Measuring Mission (TRMM) satellite precipitation radar (PR) observations, Mori et al. (2004) showed a rainfall peak traveling offshore during 2200–0400 LT at a speed of $10 \, \text{m s}^{-1}$. Kikuchi and Wang (2008) used TRMM 3B42 and 3G68 rainfall and found a similar speed of $10 \, \text{m s}^{-1}$. Mori et al. (2011) later found a slower speed of approximately $4 \, \text{m s}^{-1}$ from the West Sumatra coast using a ground-based X-band, Doppler radar. Yokoi et al. (2017)

calculated a speed of 3–3.5 m s^{-1} near the west coast of Sumatra and a faster speed of 8 m s^{-1} beyond 40 km offshore using radar observations during a pilot field campaign of the Years of the Maritime Continent Project (Pre-YMC). Fewer model studies have focused on the west coast of Sumatra. Among them, Love et al. (2011) simulated a 3–5 m s^{-1} offshore rainfall speed using WRF run with a horizontal resolution of 4 km.

There are two major physical mechanisms to explain the generation of new convection and migration of rainfall offshore at night: the land breeze and gravity waves. Over the years, people have argued over which one is the main driver. Houze et al. (1981) postulated that it was the low-level convergence between land breeze and the monsoonal flow that led to the nocturnal offshore convective propagation off the north coast of Borneo. Many other studies have also linked the evening–morning precipitation maximum over coastal ocean to convergence caused by the land or mountain breeze (Ohsawa et al. 2001; Zhou and Wang 2006; Wu et al. 2008; Park et al. 2011; Biasutti et al. 2012). Alternatively, numerous studies argue that instead of a weak land breeze, it is gravity waves that lead to the nocturnal offshore rainfall migration. Mapes et al. (2003) suggested that signals in temperature perturbation of diurnal land heating are thrust upward by the coastal topography, driving offshore gravity waves that eventually lead to offshore convection. Studies including Love et al. (2011), Yokoi et al. (2017), and Ruppert and Zhang (2019) propose that latent heating released by convection over land forces gravity waves that in turn generate convective responses. Other studies (e.g., Aves and Johnson 2008; Vincent and Lane 2016) attribute the offshore rainfall propagation to gravity waves according to the similarity of their speeds. The phase speed of gravity waves calculated theoretically by these studies range widely from 10 to 30 m s^{-1}.

In this study, we will explore the characteristics and causes of nocturnal offshore rainfall from the west coast of Sumatra using a year of ground-based radar observations and reanalysis wind and temperature fields. Data sources are further described in section 2. In section 3, the properties of offshore rainfall propagation including the frequency, speed, and intraseasonal and seasonal variations are studied. The role of the land breeze and gravity waves in offshore rainfall migration is investigated in section 4. A summary is given in section 5.

2. Data

The operational Indonesia Meteorological, Climatological and Geophysical Agency (BMKG) radar network consists of more than 30 single-polarization, Doppler C-band radars spread across the Indonesian islands. We used one year of observations from 2018 (a total of 280 days) from the BMKG radar located in Padang on the west coast of Sumatra at 0.8°S, 100.3°E (Fig. 1). The Padang radar has six elevation scan angles ranging from 0.5° to 10° and collects a full volume every 10 min. The polar coordinate radar data were interpolated to a Cartesian grid with a horizontal resolution of 1 km and a vertical resolution of 0.5 km. Radar reflectivity at 2.5 km was
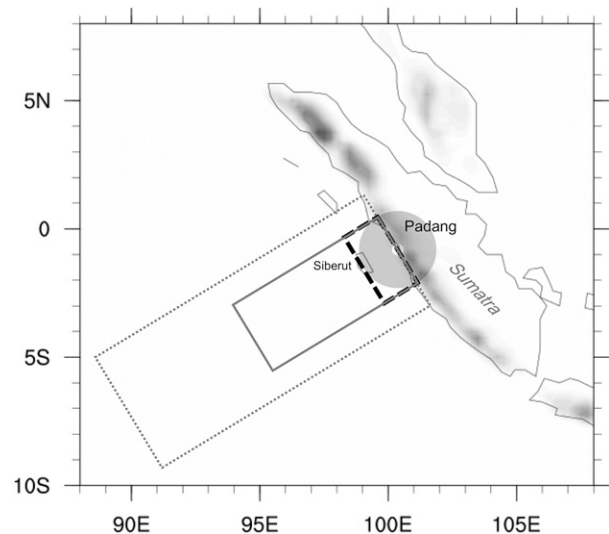

FIG. 1. Map of the BMKG Padang C-band radar region. The shaded circle indicates the 180-km radius from the radar. The dash-outlined black box marks the bounds of the short cross section perpendicular to the west coast of Sumatra, and the solid-outlined gray box marks the bounds of the long cross section perpendicular to the coast. The dot-outlined gray box indicates a larger offshore domain taken as an average background used to calculate temperature anomalies later. Topography on the islands is also shaded.

converted to rain rates using the Z–R relation, $Z = 206.2R^{1.46}$. This Z–R relation is based on Joss–Waldvogel disdrometer data collected in the Indian Ocean during the DYNAMO field campaign (Long et al. 2011; Yoneyama et al. 2013). Rain-rate retrievals were made up to 180 km from the coast of Sumatra and the 10-min rain maps were combined into hourly files. Near-surface reflectivity was further separated into convective and stratiform rain types based on the Steiner et al. (1995) texture algorithm. BMKG daily rain gauge data at Padang was used to calculate monthly rainfall during 2018.

To study diurnal circulations near Sumatra, we use wind, divergence, and temperature fields for 2018 from the ECMWF atmospheric reanalysis ERA5 (Hersbach et al. 2020). Because ERA5 analyses show discontinuities at the beginning and the end (0900 and 2100 UTC) of the 12-h assimilation cycles, especially for near-surface wind speed at low latitudes, we use ERA5 analyzed data for 0000–0600 UTC (0700–1300 LST), and ERA5 forecast data initiated at 0600 UTC (1300 LST) for 0600–2300 UTC (1300–0600 LST). ERA5 has a spatial resolution of 30 km and a temporal resolution of 1 h. Hourly surface winds observed at the Padang airport for 2018 were used to compare to and validate ERA5 low-level winds. To better isolate the propagation of features away from the coast of Sumatra, all fields (including the radar rain rates and environmental variables from ERA5) were projected on to vertical cross sections perpendicular to the coastline of Padang (the bounds of the short and long cross sections are denoted with a dashed black and solid gray box in Fig. 1, respectively). The average of all the hourly cross sections was used to represent the mean offshore propagation of each field.

3. Nocturnal offshore rainfall propagation near Padang

a. Identification of offshore events

We have two criteria to identify offshore rainfall propagation. First, rainfall propagation must be clear, continuous, and offshore. Second, offshore propagation must start after 1400 LT near the coastline of Padang to ensure that the propagation is nocturnal. We first identified cases with offshore propagation using Hovmöller diagrams of hourly rain from the Padang radar. However, the complexity of rainfall in the MC poses difficulties in identifying cases in Hovmöllers when both offshore and onshore systems exist, or when offshore propagation is weak and overwhelmed by larger-scale systems. In addition, because of the circular shape of the radar domain, offshore propagation at the upper and lower edges of the red box in Fig. 1 may arbitrarily shorten a particular feature. Therefore, movies of rain rate were used to further identify offshore propagation cases. Specifically, days with systems that propagate offshore in the radar movies were compared to their corresponding Hovmöllers. By doing this, shorter and weaker cases were also identified in the Hovmöllers. For example, Fig. 2 shows a Hovmöller of hourly radar rain rates for the first 10 days of February 2018. A shorter case was identified on 1 February and found to be at the upper edge of the radar domain from the movie. A longer and clearer case was identified on 4 February. A short case smeared by multiple systems on 7 February was observed first from radar movies and then identified in the Hovmöller. The cases on 8 and 9 February were not included because no continuous offshore propagation was observed in the radar movies, instead multiple systems showed up at different times and locations. Note that a few hours of data were missing at the end of 5 February, causing a linear artifact in the Hovmöller.

Among the 280 days of radar data obtained in 2018, 117 days were identified as having nocturnal offshore rainfall propagation (or 42% of the days). Thus, although the evening to early morning rainfall peak over coastal ocean is climatologically significant according to many previous studies (e.g., Yang and Slingo 2001; Kikuchi and Wang 2008), offshore rainfall propagation does not occur every day. The occurrence of offshore rainfall also has strong intraseasonal and seasonal variability, which will be discussed in sections 3b and 3c.

Figure 3a shows the average daily Hovmöller of total rain for all 117 events. Because of the curved coastline of Sumatra and complex rain features right at the coast, we define the starting point of offshore rainfall as 10 km away from the coastline. Offshore rainfall starts near the coast at around 1800 LT, and propagates seaward with a mean speed of 4.5 m s^{-1} within 180 km offshore of Padang, more consistent with recent studies using local or spaceborne radar (e.g., Mori et al. 2011; Yokoi et al. 2017) or high-resolution models (e.g., Love et al. 2011). Figure 3a also shows a strong local precipitation peak at 1300 LT 150–180 km away from Sumatra, which is caused by afternoon convection over Siberut Island off the coast of Padang (Fig. 1). Siberut Island has a secondary precipitation peak at 0300 LT, corresponding to the rainfall resulting from systems propagating offshore from Sumatra overnight. The magnitude of the secondary peak is about one-fourth of the primary peak.
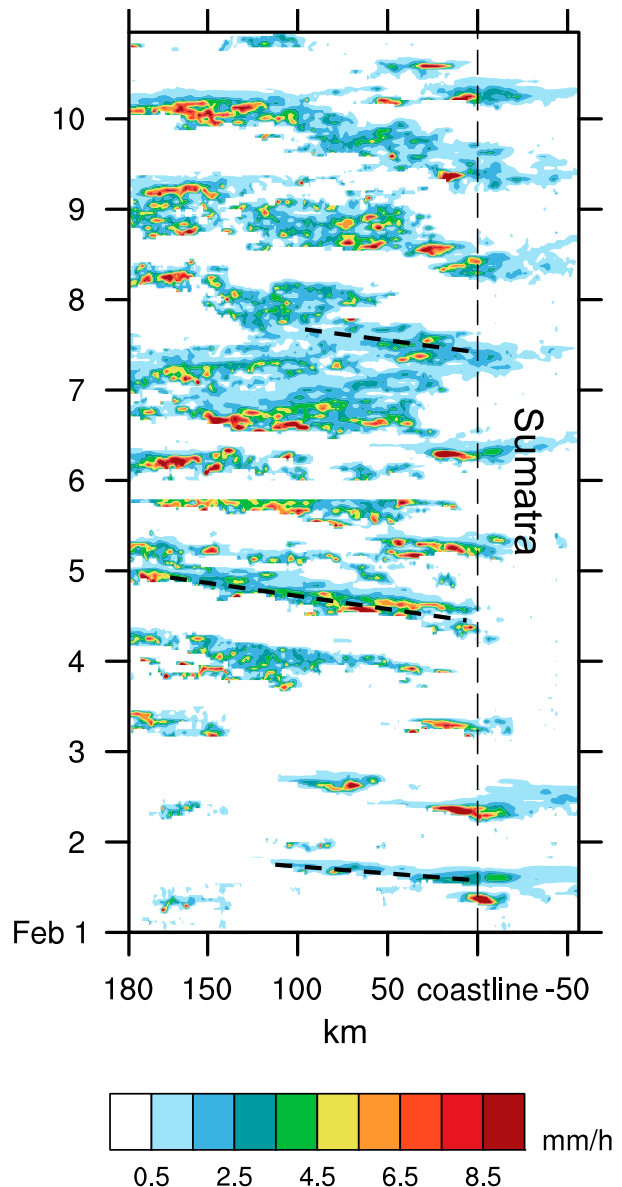

FIG. 2. Hovmöller diagram of hourly rain rate from the Padang radar for the first 10 days of February 2018. The dates are in UTC. Rain rate is averaged along the wider dimension of the dashed black box in Fig. 1. The vertical dashed line represents the coastline, with water on the left and Sumatra on the right. Thick black dashed lines denote the three offshore rainfall propagation events identified during the 10 days.

Figure 3b shows the average daily Hovmöller of total rain for the 163 days without nocturnal offshore rainfall propagation. There is less overall rainfall off the coast of Sumatra when offshore propagation is absent. In addition, the two precipitation peaks over Siberut are weaker than in Fig. 3a. Figures 3c and 3d show the ERA5 900-hPa flow in the vicinity of Sumatra for days with and without offshore rainfall events, respectively. Comparison of the maps indicate that stronger westerly low-level winds coincide with days without offshore rainfall events.
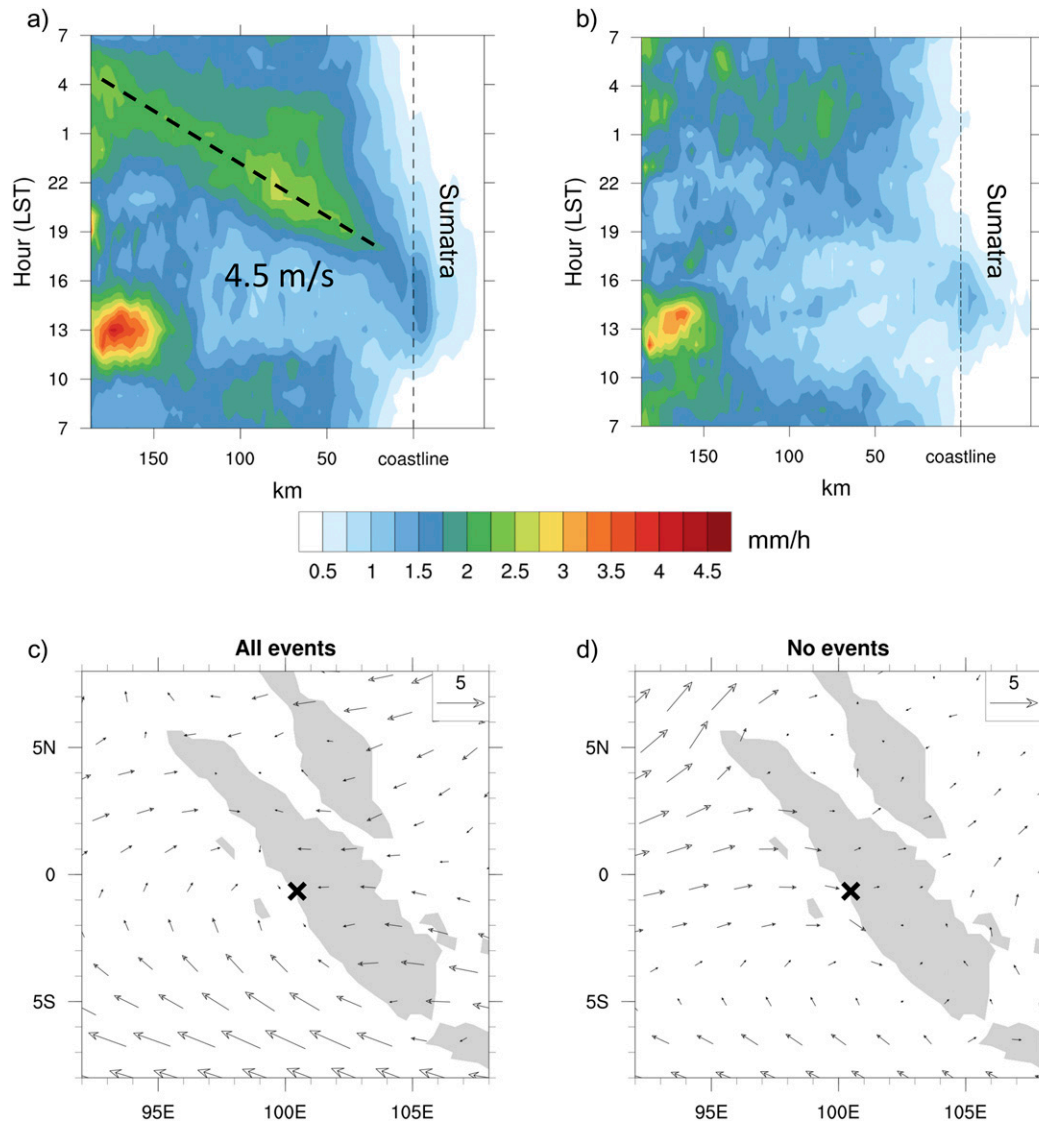
FIG. 3. (a) Hovmöller diagram of the average rain rate of all 117 offshore rainfall propagation events identified during 2018. Time is in LST. The thick black dashed line indicates the propagation speed of the rainfall (4.5 m s^{-1}). (b) As ins (a), but for days without offshore rainfall propagation. Also shown are large-scale wind maps at 900 hPa averaged for all the days (c) with and (d) without offshore propagation events. Black crosses mark the location of Padang.

The large-scale circulation over Sumatra varies intraseasonally and seasonally; thus, offshore rainfall event occurrence may be expected to vary because of changes in the large-scale environment associated with the MJO and monsoons as described in the next two sections.

b. Intraseasonal variations

The diurnal cycle over the MC interacts strongly with the passage of the MJO, which may in turn imply an intraseasonal variation in offshore rainfall propagation. Offshore event occurrence was separated into different MJO phases based on the Wheeler and Hendon (2004) real-time multivariate MJO index (RMM) and the Liu et al. (2016) revised RMM index

(RMM-r), which weights OLR (and thus convection) more heavily than the 850- and 200-hPa winds compared to the Wheeler and Hendon RMM index. Figure 4 shows a histogram of nocturnal offshore-propagating event occurrence based on each index. The 900-hPa winds from ERA5 during 2018 are plotted in Fig. 5 to show the large-scale circulation variations in the vicinity of Sumatra during the evolution of the MJO.

According to both indices, most events take place during phases 1–3 (Fig. 4) when the MJO is active in the Indian Ocean and 900-hPa flow near the coast of West Sumatra is transitioning from offshore to onshore as the MJO approaches the MC (Fig. 5). Almost no offshore-propagating events occur in
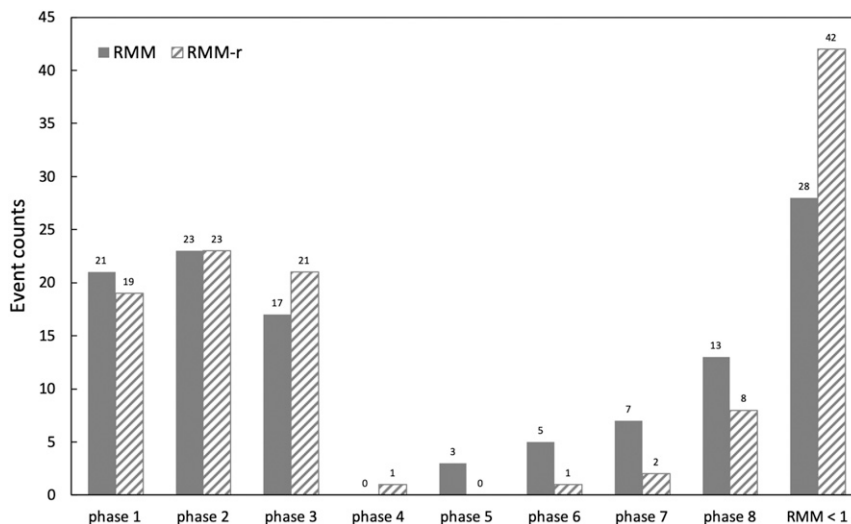
FIG. 4. Offshore rainfall propagation occurrence from Padang during 2018 in each MJO phase. Event counts that are based on RMM (Wheeler and Hendon 2004) are solid, and those that are RMM revised (Liu et al. 2016) are hatched. RMM < 1 means that the MJO was weak.

phases 4 and 5, when the MJO is active over the MC and 900-hPa flow over Sumatra is strong and westerly. There is a gradual increase in offshore event occurrence from phases 6 to 8 when the MJO propagates eastward over the Pacific and low-level flow over West Sumatra weakens and transitions from onshore to offshore. A significant number of offshore-propagating events also occur when the RMM or RMM-r value is less than 1, indicating a weak MJO. The 900-hPa flow during weak MJOs is weakly onshore, and most similar to the wind field of phases 6–7.

Therefore, strong westerly low-level winds appear to prevent the land convection from propagating offshore during the active MJO, whereas weaker low-level onshore flow appears to promote offshore rainfall events when the MJO is approaching Sumatra, or when the MJO circulation does not predominate. Using TRMM 3B42 data, Ichikawa and Yasunari (2006, 2007) documented that the nocturnal rainfall propagation speed over the MC islands is modulated strongly by low-level easterlies and westerlies in different MJO regimes. Ruppert and Zhang (2019) and Ruppert et al. (2020) proposed that zonally propagating systems under easterly and westerly MJO regimes may be related to diurnal gravity waves generated primarily by convection based on a cloud-permitting model. Similar to the MJO, large-scale systems such as cold surges may also impact the occurrence of offshore events by affecting the large-scale environment (Yokoi et al. 2019).

Figure 4 indicates that both indices show a consistent relationship between MJO phase and nocturnal offshore propagation. However, more events are identified during active MJO periods using the RMM index, which may be due to the stronger weighting of low-level winds by the RMM index and the fact that the low-level winds vary significantly over the west coast of Sumatra during the evolution of the MJO. Another point of interest is that precipitation increases over West Sumatra and just off its coast ahead of the main body of the

active MJO during phases 1 and 2 (Peatman et al. 2014). We suggest that offshore-propagating systems likely play a role in the rainfall signal off the west coast of Sumatra during these phases and that they may help create a more conducive, moist environment for the MJO as it approaches the MC.

c. Seasonal variations

The MC is under the strong influence of the Asian and Australian monsoons, which impact atmospheric circulations and moisture supplies seasonally. December–February (DJF) and June–August (JJA) are the Australian and Asian summer monsoon seasons, respectively. March–May (MAM) and September–November (SON) are considered to be transition seasons. Figure 6 shows the monthly rain gauge measurements during 2018 at Padang (indicated by the line). Padang is rainy throughout the year (i.e., monthly mean values are greater than 160 mm), but rainfall decreases when the monsoons are active to the south and north and increases during the transition seasons.

Figure 6 also shows the frequency of nocturnal offshore propagation events by month in 2018. Percentage relative to all available days is used instead of counts because of missing radar data in each month: 20 days in DJF, 10 days in MAM, 30 days in JJA, and 16 days in SON. The two transition seasons have the highest frequency of offshore rainfall propagation, with a maximum daily occurrence of 80% in October. JJA has the lowest frequency with a daily occurrence around 20%. The annual cycle of monthly frequency of offshore rainfall propagation from Padang is generally consistent with the monthly rain gauge climatology, implying that the occurrence of offshore propagation events is associated with the amount of rainfall received on land.

According to section 3b, MJO activity also contributes to the frequency of nocturnal offshore rainfall propagation so months containing MJO phases 4 and 5 (when the MJO is active over
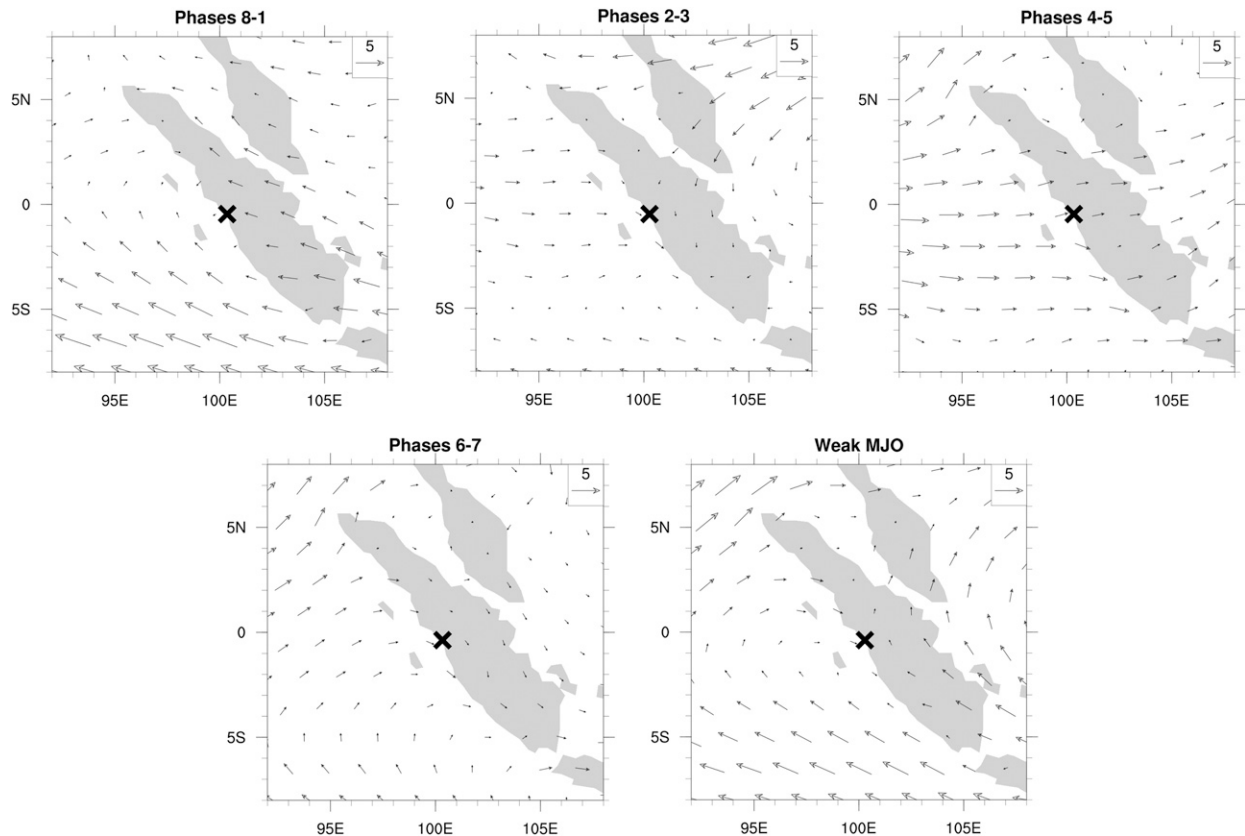
FIG. 5. ERA5 synoptic winds at 900 hPa for days in 2018 categorized into MJO phases and the weak MJOs. Black crosses mark the location of Padang.

the MC and offshore rainfall propagation is almost nonexistent) are denoted with an asterisk in Fig. 6. While MJO phases 4 and 5 occurred in many of the monsoon months during 2018, potentially contributing to the lower offshore event occurrence, these MJO phases also occurred in transition months with relatively high offshore propagation occurrence (e.g., May).

Figure 7 shows synoptic winds near Sumatra at 900 hPa from ERA5 for the four seasons. In DJF, northeasterly monsoon flow from Asia shifts to northwesterly after crossing the equator and in JJA, southeasterlies from Australia also shift to northwesterlies in the Northern Hemisphere. In MAM and SON, winds are weaker near the equator relative to the monsoon seasons but maintain a landward component off the coast of Padang. Thus, the percent of events may also be affected by the synoptic winds in which weaker onshore winds are less likely to counteract the seaward propagation of rainfall systems during the transition seasons of MAM and SON.

The 117 nocturnal offshore-propagating events were categorized into the four seasons. A total of 18 offshore rainfall events occurred in DJF, 37 in MAM, 12 in JJA, and 50 in SON. The top row of Fig. 8 shows daily Hovmöller plots of total rain for the identified offshore propagation events in each season. The Asian monsoon season (DJF) has a clear nocturnal offshore rainfall migration starting near the coast at around 1800

LT, with a propagation speed of approximately $4.5 \, \mathrm{m \, s^{-1}}$. The largest rain rate is found 70 km away from the coast; the distance that offshore rainfall can reach may be associated with humidity and temperature at the top of the coastal boundary layer (Coppin and Bellon 2019). In the Australian monsoon season (JJA), the offshore rainfall also starts at 1800 LT but propagates for a shorter distance compared to DJF, possibly due to the relative dryness in this season. The propagation speed in JJA is approximately $5.5 \, \mathrm{m \, s^{-1}}$.

The transition season of SON experiences almost half of the events and the clearest-propagating signal (Fig. 8). Offshore rainfall starts at 1800 LT and propagates at roughly $5.0 \, \mathrm{m \, s^{-1}}$, consistent with the offshore events during the monsoon seasons. Although MAM experiences more complex rainfall features, an offshore propagation that starts at 1700 LT, slightly earlier than the other seasons, and migrates seaward at $4.0 \, \mathrm{m \, s^{-1}}$ can still be identified. A faster but less coherent propagation signal is also evident during MAM. When cases were examined individually, this fast propagation was found in only 2 of the 37 events. Because of the low frequency of the faster propagation events, we will focus on the propagation at $4.0 \, \mathrm{m \, s^{-1}}$.

Few previous studies have looked explicitly at whether there is a difference in the offshore propagation of convective and stratiform rain. In this study, the total radar rain was separated
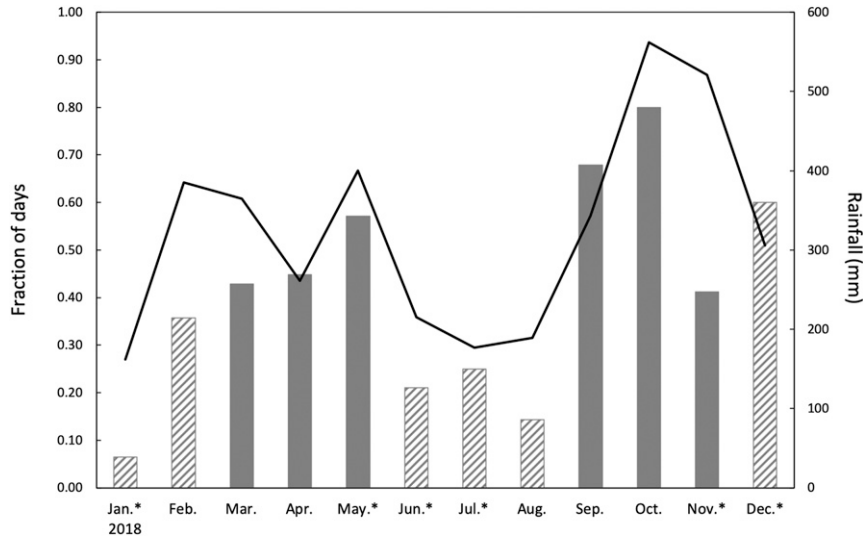
FIG. 6. Fraction of days with offshore rainfall propagation from Padang in each month during 2018. Monsoon- and transition-season months are dashed and solid filled bars, respectively. Asterisks mark months with the presence of MJO phases 4 and 5. The line represents the 2018 monthly rain gauge at Padang.

into convective and stratiform components based on Steiner et al. (1995). The middle and bottom rows of Fig. 8 show daily Hovmöllers of seasonally averaged convective and stratiform rain during offshore propagation events with propagation speeds estimated in a similar fashion as for the total rain. A summary of offshore propagation speed for each rain type and season can be found in Table 1. In all four seasons, the propagation speed of convective rain is indistinguishable from the total rain since the total rain is composed mostly of convective rain, especially closer to the coast. Stratiform rain propagates seaward faster than convective rain and dominates farther away from the coast, likely due to the mesoscale organization of the convective systems with time (e.g., Houze et al. 1981). To check the robustness of the faster stratiform rain speed, the convective and stratiform rain propagation speeds of all offshore rainfall cases were compared event by event. Cases with faster stratiform rain propagation account for approximately 74% of the events, and roughly 10% of the cases had equal convective and stratiform rain speeds. Only 16% of the convective cases were faster. Stratiform anvil clouds cover large areas and look highly reflective to satellites. The different propagation speeds of convective and stratiform rain in our study may explain why passive satellite instruments observe a faster offshore migration compared to radar. Cause for the different speeds of convective and stratiform rain will also be discussed in section 4.

4. Offshore propagation formation mechanisms

There is much debate in the community on whether land breezes or gravity waves are more important in generating new convection near coastlines and in driving nocturnal offshore rainfall migration in the tropics. According to linear theory, the land–sea-breeze circulation can be seen as a gravity wave response to a diurnally oscillating land–sea temperature gradient (Rotunno 1983). However, near the coast, nonlinearity due to boundary layer effects and orographic forcing are involved in the land–sea-breeze circulation, whose propagation speed is slower relative to farther offshore (e.g., Vincent and Lane 2016; Short et al. 2019). Gravity waves can also be generated by convection over land. Therefore, we attempt to distinguish between the land breeze and other gravity wave responses in this study.

a. Land breeze

It has been argued that there should be little to no land breeze over tropical regions because of the weak temperature contrast between land and nearby water at night (e.g., Mapes et al. 2003), so we first investigate the surface winds at Padang to see if a diurnal shift in wind is apparent. Figure 9 shows day (0700–1900 LT) and night (1900–0700 LT) time wind roses from in situ BMKG surface observations at the Padang airport and the ERA5 10-m wind at the closest point to the airport for July and October (months that represent the seasons with the fewest and the most offshore propagation events, respectively; Fig. 6). Figure 9 shows that onshore winds dominate during the day and shift to offshore at night in both months and for both observations and reanalysis, indicating that a diurnal temperature contrast exists to support a land breeze regardless of different offshore rainfall propagation event frequencies. Moreover, variations in the direction of the onshore and offshore winds reflect seasonal changes of the background flow seen in Fig. 7.

Considering the relatively coarse 30-km resolution of ERA5 compared to a point measurement and the resulting approximate representation of the coastline and mountains in ERA5, we do not expect the wind roses from the BMKG surface site and ERA5 to be a perfect match. For example, the ERA5 wind
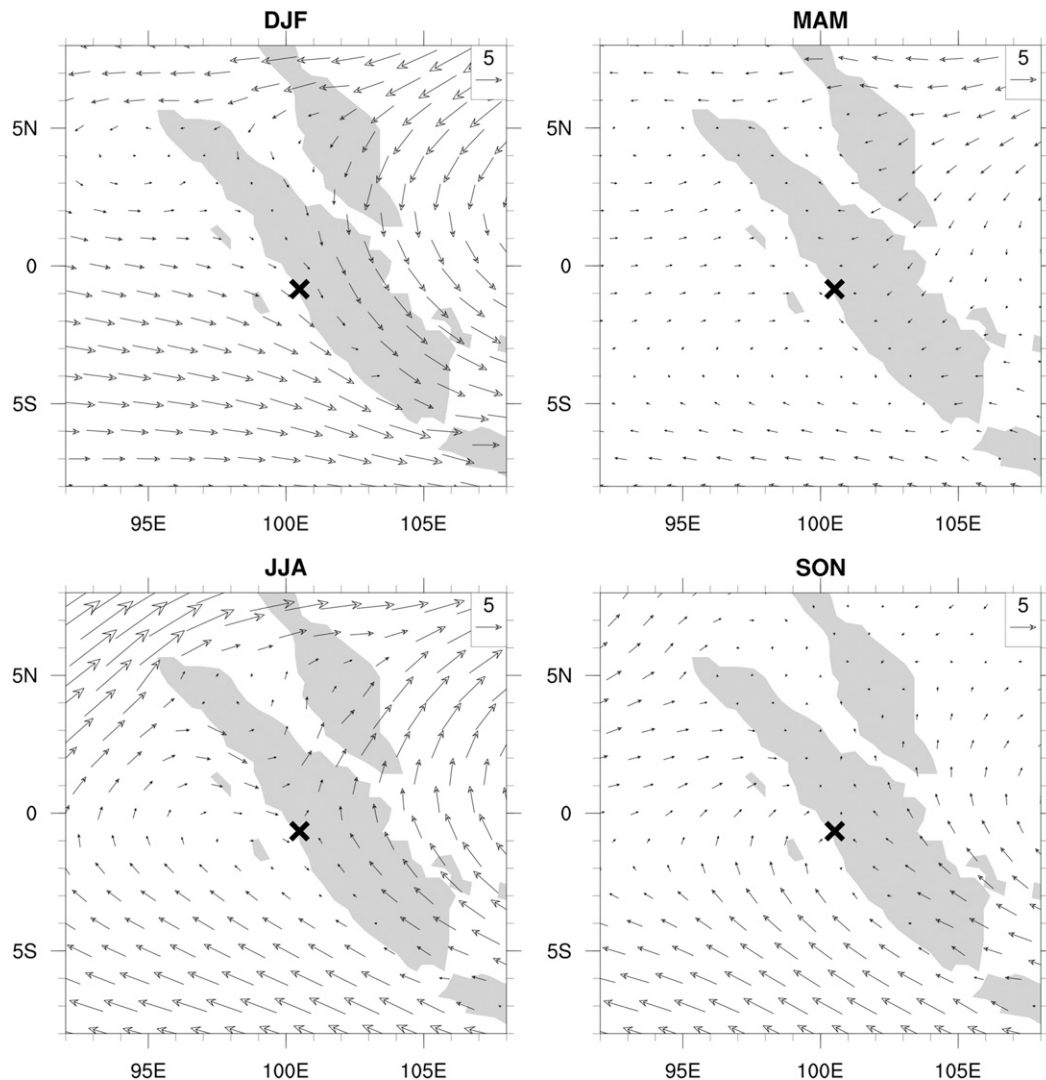
FIG. 7. ERA5 synoptic winds near Sumatra at 900 hPa by season. Black crosses mark the location of Padang.

speeds are generally smaller than the airport surface observations in Fig. 9, likely because point measurements can attain higher wind values than winds smoothed over a larger region. However, calm winds (less than $0.5 \, \mathrm{m \, s^{-1}}$) at night account for over 60% of the observed surface winds in both months, while many fewer occurrences of calm wind are found in ERA5 10-m winds. This difference can also be argued to be due to resolution differences since calm winds are less likely to be consistently observed over larger averaging regions. In addition, a relatively higher frequency of northerly winds is observed by the BMKG surface station at night in both months (and throughout the year—not shown), which may be due to mesoscale processes associated with the local topography that are captured by ERA5 with a wider range of direction and speeds from the north-northwest. More details on the comparison of ERA5 near-surface winds with observations and with other reanalysis products can be found in Ramon et al. (2019) and Belmonte Rivas and Stoffelen (2019). In summary, while the

30-km resolution of ERA5 is inadequate to resolve the land breeze front and other finescale features observed by the Padang surface station, it appears able to capture the diurnal wind shift that is broadly consistent with the surface observations. Thus, we will use ERA5 winds to investigate the relationship between offshore rainfall propagation and the land breeze near Padang.

Land–sea breezes are diurnally asymmetric, with the land breeze having a much weaker magnitude compared to the sea breeze. In our case, the land breeze is typically less than $3 \, \mathrm{m \, s^{-1}}$ year round, which is why some previous studies have argued that land breezes are too weak to drive offshore rainfall propagation. However, it is not the land breeze itself that drives offshore rainfall propagation; low-level convergence is needed to generate new convective cells.

Houze et al. (1981) suggested that low-level convergence between the southeasterly land breeze off the north coast of Borneo and the northeasterly monsoon flow is the driver of
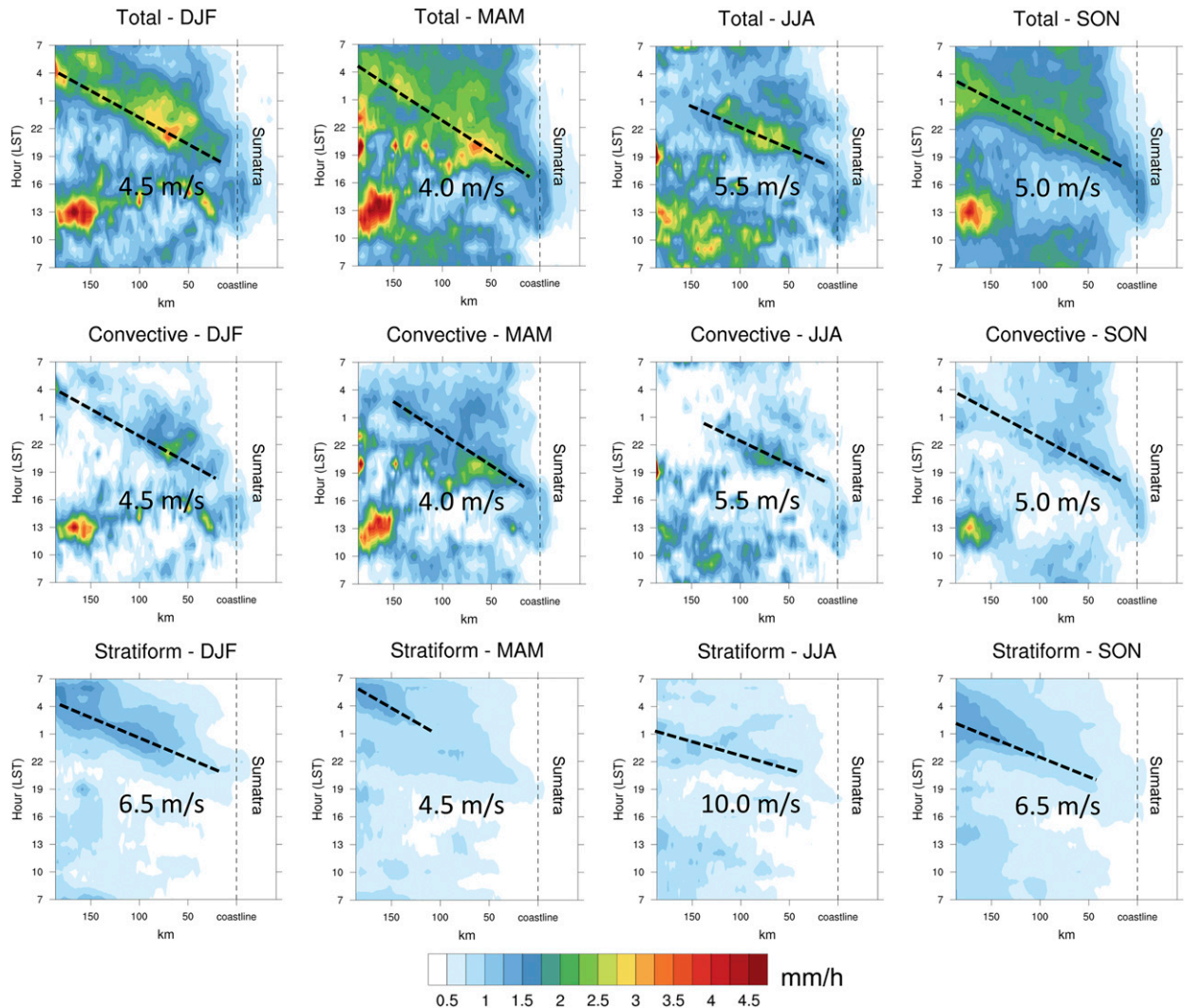
FIG. 8. As in Fig. 3a, but the Hovmöller diagrams are categorized by season (columns) and rain type (rows) for the identified offshore propagation events. The number of events in DJF, MAM, JJA, and SON is 18, 37, 12, and 50, respectively. Shown are (top)the total rain in each season, (middle) convective rain, and (bottom) stratiform rain. Thick black dashed lines of propagation and their speeds are overlaid on each panel.

offshore convection propagation northward from Borneo. This explanation was disputed by Mapes et al. (2003), who argued that the land breeze and monsoon flow observed north of Borneo is perpendicular to each other and cannot generate convergence. However, the background winds in our case often have a landward (westerly) component that may create convergence when coupled with the land breeze.

To assess whether low-level convergence is associated with the nocturnal offshore rainfall propagation observed by the Padang radar, Fig. 10a shows the Hovmöller of ERA5 divergence at 975 hPa for all 117 offshore events. Convergence propagates offshore at a speed of 5.5 m s^{-1}, starting just before the rainfall propagation in Fig. 3a suggesting that low-level convergence may be forcing convective development. However, low-level convergence can also be a result of convection. Since it is difficult to separate the convergence

caused by convection from that associated with the land breeze, we looked at convergence propagation on days with neither offshore rainfall propagation nor MJO phases 4–6 (i.e., when we saw the strongest influence of the MJO on offshore rainfall migration). Figure 10b shows that low-level

TABLE 1. Approximate speeds of nocturnal offshore propagation of rainfall and convergence (in m s^{-1}) from Padang. The "total" column is boldfaced for emphasis.

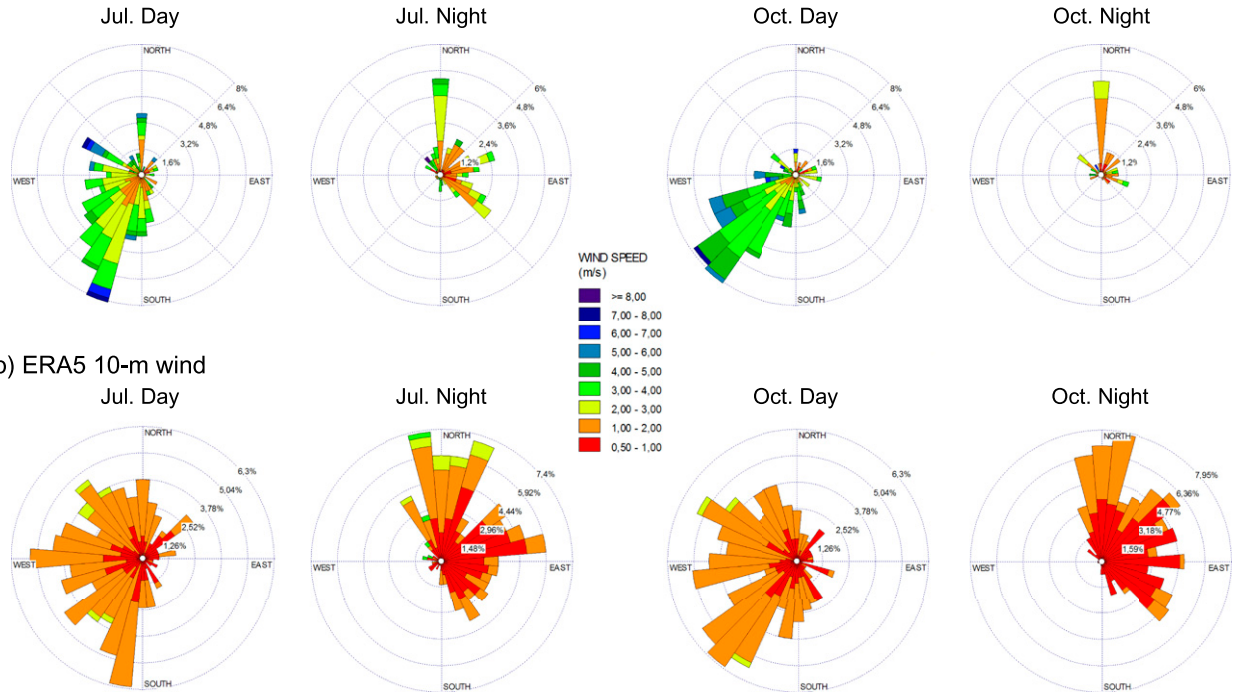|	Total	DJF	MAM	JJA	SON
No. of events	**117**	18	37	12	50
Total rain	**4.5**	4.5	4.0	5.5	5.0
Convective rain	**4.5**	4.5	4.0	5.5	5.0
Stratiform rain	**6.0**	6.5	4.5	10.0	6.5
ERA5 975-hPa convergence	**5.5**	5.5	6.0	5.0	5.5

a) BMKG surface observations

b) ERA5 10-m wind

FIG. 9. (a) Wind roses from the BMKG surface station at the Padang Airport (0.8°S, 100.3°E) for day (0700–1900 LT) and nighttime (1900–0700 LT) in July and October 2018. (b) The corresponding ERA5 10-m wind roses at 0.75°S, 100°E. Wind speed ranges are indicated with colors. The frequency of the wind direction is shown by the length of the "rose petal." Note that calm winds ($<0.5\,\mathrm{m\,s^{-1}}$) are ignored.

convergence propagates offshore even when nocturnal offshore-propagating events do not occur. While the low-level convergence in Fig. 10b has the same propagation speed as in the propagating rainfall events, it has a smaller amplitude. We thus propose that the convection is likely initiated by convergence associated with the land breeze, but that the convection itself then acts to amplify this convergence as time evolves. Using an idealized model, Qian et al. (2012) point out that coastal land terrain tends to enhance the land breeze because the daytime sea-breeze density current is blocked by the mountains and a pool of cool air accumulates at the base of the topography. This air cools further at night and enhances the temperature contrast between land and water, producing a stronger land-breeze density current. In our case, coastal topography along West Sumatra (Fig. 1) may play a role in strengthening the land breeze. In addition, precipitation can lead to near-surface evaporative cooling once formed, which may contribute to the strengthening of the density current as well. In this sense, the offshore rainfall may speed up its own propagation.

To further bolster our arguments, diurnal winds normal to the coast at 975 hPa corresponding to the divergence fields in Figs. 10a and 10b are shown in Figs. 10c and 10d. Offshore wind starts near the coastline at 1800 LT in both cases, in agreement with Gille et al. (2005) who showed that the maximum land breeze closest to the west coast of Sumatra occurs between 1600 and 2000 LT. The propagation lines associated with the low-level convergence (repeated on the wind anomaly plots)

fit well with the lines of zero speed, indicating that the offshore convergence is caused by the offshore land breeze in the evening along with the onshore component of the prevailing wind.

The density current speed V may be estimated theoretically from ERA5 data based on Benjamin (1968), Simpson and Britter (1980), and Seitter (1986). The height of the land breeze H is concentrated in the lowest 1 km, the cold air temperature T_c at the base of the west Sumatra topography at night (1900–0100 LT) is estimated to be 298 K, the ambient air temperature T_w is roughly 299 K, and the background wind $\overline{U}$ is approximately $-0.7\,\mathrm{m\,s^{-1}}$ (minus sign means the background wind is in the opposite direction of the density current). Using $V = k[gH(T_w - T_c)/T_c]^{1/2} + 0.62\overline{U}$, where k is a constant ranging from 0.7 to 1.08 for the atmosphere (Wakimoto 1982), the density current speed from west Sumatra is estimated to be between 3.6 and $5.8\,\mathrm{m\,s^{-1}}$, broadly consistent with the $5.5\,\mathrm{m\,s^{-1}}$ observed.

There is also a seasonal variation in convergence propagation speed off the coast of Sumatra. Table 1 shows that the propagation speed of the offshore convergence ranges from 5.0 to $6.0\,\mathrm{m\,s^{-1}}$, while the convective rain propagation is consistently slower by $1.0\,\mathrm{m\,s^{-1}}$ on average. In theory, the convective system as a whole would have to propagate at the same speed as the convergence front. A few reasons may explain the small speed difference. First, as mentioned before, ERA5 divergence is largely set by temperature contrast and may not capture the frontal propagation very well due to its coarse resolution.
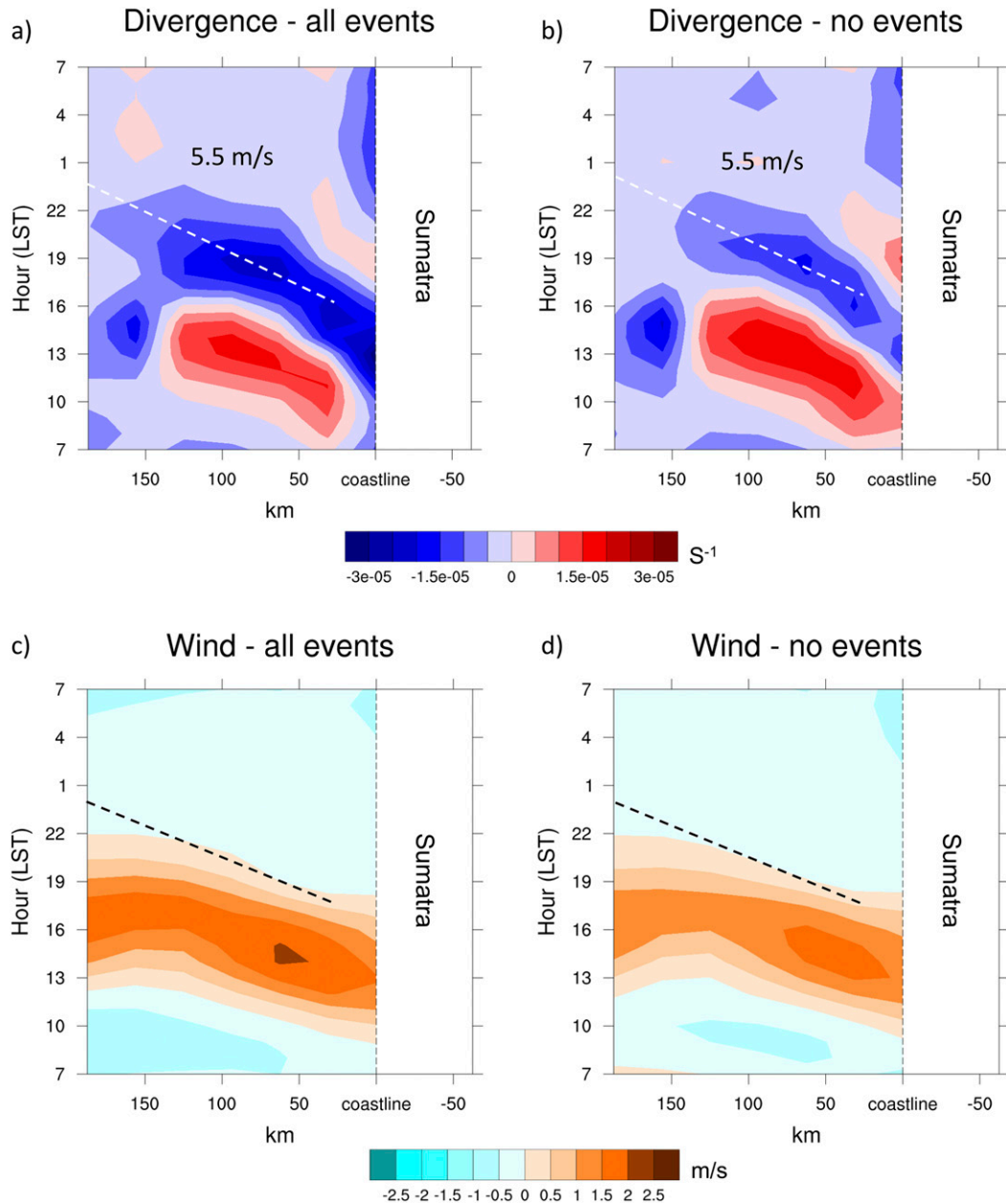
FIG. 10. As in Fig. 3, but for ERA5 975-hPa (a),(b) divergence and (c),(d) coast-normal winds. Onshore winds are positive. Terrain on Sumatra is higher than 975 hPa so the right side of the coastline is masked. Thick black dashed lines on bottom panel are copied from top panel.

Second, as in Figs. 8 and 10a,b, the slower propagation speed closer to the coast poses difficulty drawing lines of constant speed for both radar rain and convergence, in other words, it is not immediately obvious what the precise propagation speed should be.

b. Background winds

As shown in Fig. 8 and summarized in Table 1, the stratiform rain offshore propagation is faster than the convective rain offshore propagation throughout the year. Houze (1997)

discussed that deep convective cloud bases reside in the lower troposphere, while stratiform rain that forms from deep convection has its cloud base in the midtroposphere. Thus, background winds that vary in the vertical may cause the convective and stratiform rain propagation speeds to be different.

Figure 11 shows vertical profiles of the coast-normal component of the nocturnal background wind in each season. The background wind was calculated over a region offshore from Sumatra (see the dashed black box in Fig. 1) between 1500 and 0700 LT from ERA5. Figure 11 indicates that low-level
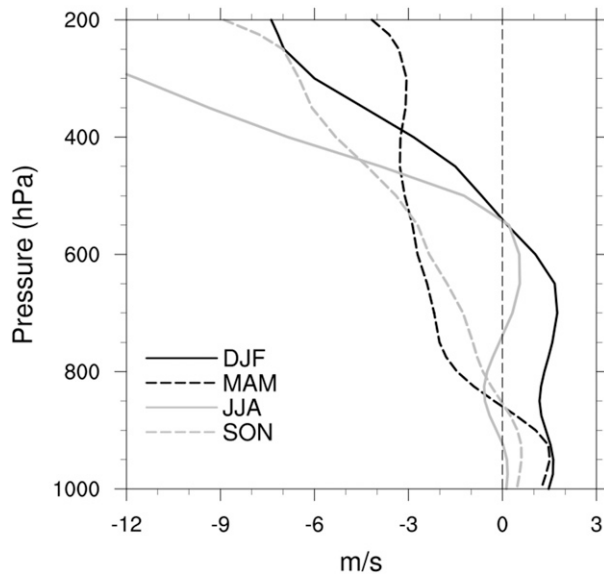
FIG. 11. Seasonal vertical profiles of the coast-normal component of the background wind from ERA5 averaged over the black dash-outlined box in Fig. 1 from 1500 to 0700 LT.

background winds are generally positive (i.e., onshore) and help to form the low-level convergence with the land breeze that causes convection to propagate offshore. However, upper-level background winds are negative (i.e., offshore) with varying amounts of shear. A comparison between Fig. 11 and Table 1 shows that seasons with stronger upper-level shear have larger differences between the convective and stratiform rain propagation speeds. This holds especially true for JJA. We argue that the upper-level winds increase the propagation speed of the stratiform rain compared to the convective rain during nocturnal offshore events from the coast of Sumatra.

A schematic in Fig. 12 is shown to demonstrate this mechanism more clearly. When new offshore convection is generated by the low-level convergence formed at the intersection of the land breeze and background low-level winds, the propagation speed of the convective cells (yellow shading and arrow) is set by the propagation of the convergence zone (red arrow). However, upper-level easterly winds speed up the offshore stratiform rain (green shading and arrow) relative to the convective cells initiating at the convergence zone, thus accounting for why stratiform rain propagates faster than convective rain. Figure 12 also shows storm-relative, coast-normal background wind speeds averaged for all events (blue arrows). Taking the storm motion into account, there exists front-to-rear low-level winds, weak midlevel winds, and rear-to-front upper-level winds. Parker and Johnson (2000) showed that this storm-relative wind profile leads to stratiform clouds expanding ahead of convective clouds in midlatitude mesoscale convective systems, consistent with our observations off the coast of Sumatra. While we assume that the stratiform rain propagation speed will always exceed the convective rain propagation speed in these conditions, the actual increase in stratiform rain propagation speed will vary because the stratiform rain

propagation speed also depends on the precipitation efficiency of the stratiform cloud (i.e., whether it rains out rapidly or is allowed to be advected far away from the parent convective cells by the upper-level wind before fully precipitating out).

c. Gravity waves

Previous studies have shown that gravity waves have the potential to affect offshore convection propagation (e.g., Mapes 1993; Mapes et al. 2003; Love et al. 2011; Du and Rotunno 2018). To explore the role of gravity waves in offshore rainfall migration, Fig. 13 shows vertical cross sections of the diurnal cycle of ERA5 temperature anomalies averaged for all events up to 800 km offshore of Sumatra (i.e., averaged along the narrow dimension of the gray-outlined box in Fig. 1). Temperature anomalies are calculated at each level at each time against an average background temperature (which is taken over a larger offshore domain indicated by the dot-outlined gray box in Fig. 1 to diminish the strong coastal influence on temperature). By taking temperature anomalies at each time, the diurnal cycle is partially taken out so that gravity waves can be more clearly seen.

As seen in Fig. 13, the temperature disturbance begins as a warm anomaly over the coastal mountains near noon. As time evolves, the anomaly then propagates offshore, particularly below 850 hPa. The amplitude of the anomaly weakens with time, but the disturbance is still clearly identifiable as late as 0400 LT the following morning, at a distance of over 400 km from the coast. Tracking the position of the disturbance with time suggests a propagation speed of roughly $8\,\mathrm{m\,s}^{-1}$ (the thick black dashed line in Fig. 13), which is faster than both the rainfall propagation in Fig. 8 and the propagation of the convergence zone/land-breeze front in Fig. 10, indicating that the convergence propagation speed is a better match to the convective rain. In addition, the relatively constant propagation speed of the offshore temperature anomaly cannot explain the speed transition of the offshore rainfall from slow to fast with distance from the shore, which will be discussed in section 4d. At later times (after roughly 1900 LT), a cold anomaly appears above the warm disturbance and appears to propagate offshore as well. At times, the appearance of the cold anomaly suggests a line of constant phase extending upward and away from the coastline, as suggested by the dotted red line for 1900–0100 LT in Fig. 13.

Several mechanisms come to mind to explain the propagation of the temperature anomaly seen in Fig. 13. The first is that the disturbance is simply the direct impact of the propagating convection on the temperature field, as caused by the effects of diabatic heating. However, as seen in the figure, the positive part of the temperature anomaly is largely limited below 850 hPa, which would appear too low to reflect the effects of convection. Furthermore, the propagation speed of the anomaly exceeds that of the rainfall signal, as noted above. A second explanation is that the disturbance reflects the effect of a gravity wave produced by the propagating land breeze front (i.e., a wave stationary in the frame of the front). However, while such a wave may indeed exist, the propagation speeds are again different. We thus hypothesize that the most likely explanation is that the disturbance reflects a gravity wave generated over land during the
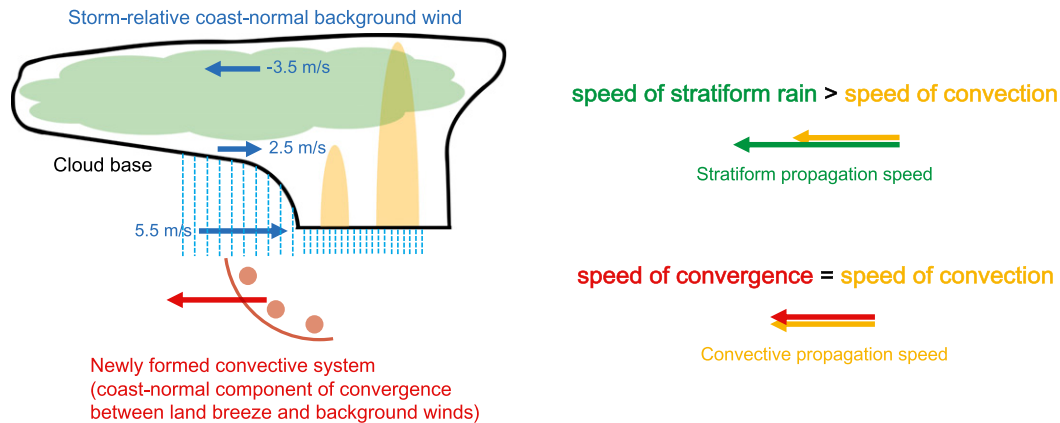
FIG. 12. Schematic to explain how low-level convergence drives offshore rainfall propagation and the influence of the vertical profile of winds on the propagation speed for different rain types. The system's leading edge is to the left. The low-, mid-, and upper-level storm-relative winds are calculated at 1000–900, 650–550, and 300–200 hPa, respectively.

afternoon hours, due to convection over the coastal topography. A warm anomaly is also seen above the cold anomaly mentioned above (not shown), indicating a high-order gravity wave structure whose vertical wavelength is two thirds the height of the troposphere (Mapes 1993). As time evolves, the wave then propagates offshore, ahead of both the land breeze front and the propagating convection.

From Fig. 13, the vertical wavelength of the disturbance is estimated to be roughly 4 to 5 km. Given the observed static stability of approximately $0.0125\,\mathrm{s}^{-1}$ and low-level background wind (cf. Fig. 11), this suggests both phase and group speeds of roughly 6.5–$8.5\,\mathrm{m\,s}^{-1}$, which is broadly consistent with the estimate given above. Ruppert and Zhang (2019) identified a gravity mode with a similar phase speed near Sumatra based on high-resolution model experiments, which they loosely attributed to the propagating convective heat source. Regardless of the mechanism, it would appear from Fig. 13 that the propagating mode has the effect of destabilizing the lower to mid-troposphere, thus modulating the environment ahead of the propagating rainfall signal to be more favorable for convection.

Note also that the gravity wave response associated with coastal heating is often modeled in terms of a steadily oscillating, diurnal heat source, in which all components of the wave oscillate at the same (ground relative) frequency (e.g., Rotunno 1983; Qian et al. 2009; Du et al. 2019). However, even when background winds are included, such steadily oscillating models typically do not feature propagating modes, like that seen in Fig. 13. One possible explanation is that the real problem features a range of higher-frequency components, in addition to the diurnal oscillation, particularly due to the influence of convection over the coastal mountains. In that sense, it seems possible that a better conceptual model is the response to an instantaneously pulsed or rapid-onset heat source (e.g., Dickinson 1969; Mapes 1993), reflecting the fairly rapid appearance of convection in the late morning/early afternoon.

d. Offshore rainfall propagation at different distances

We only assessed offshore rainfall within 180 km from Padang; rainfall farther offshore is beyond the scope of this study because it is out of radar range. However, a short discussion on offshore rainfall at distances beyond 180 km will be given here for completeness. Previous studies have shown that the late evening to early morning precipitation maxima over coastal oceans reach as far as many hundreds of kilometers and propagate faster farther offshore. For example, using WRF, Vincent and Lane (2016) pointed out that precipitation propagates at 3–$5\,\mathrm{m\,s}^{-1}$ 100–200 km from the northeast coast of New Guinea and at $18\,\mathrm{m\,s}^{-1}$ farther offshore. They suggested that the slower rainfall propagation is driven by the land-valley breeze while the faster propagation is driven by gravity waves. Based on satellite scatterometer measurements, Short et al. (2019) found that land breezes propagate at a slower speed of $8\,\mathrm{m\,s}^{-1}$ near the coast of southwest Sumatra, but at 25–$30\,\mathrm{m\,s}^{-1}$ beyond 200 km as gravity waves. In addition, the $0.5\,\mathrm{mm\,h}^{-1}$ precipitation contour near the coast overlaps the transition point between onshore and offshore winds, in agreement with our Fig. 10. In this study, it is also worth noting that the propagation speed of convergence becomes faster beyond 100 km in Figs. 10a and 10b, implying that the land breeze becomes less important at this distance. Previous satellite IR studies have seen a faster offshore rainfall speed on the order of 10–$15\,\mathrm{m\,s}^{-1}$ (see introduction for details), while recent local or spaceborne radar studies, including the C-band radar used here, have observed a slower speed on the order of $5\,\mathrm{m\,s}^{-1}$. A larger proportion of stratiform rain with a faster speed is found beyond 150 km offshore from Sumatra (bottom row in Fig. 8), and the predominance of stratiform rain in offshore rainfall has also been reported by other studies (e.g., Houze et al. 1981; Ruppert and Zhang 2019). The fact that upper-level easterly winds speed up the stratiform rain (section 4c) partially explains the offshore propagation speed discrepancy with previous satellite IR studies, where high reflective clouds are observed. Another key to the discrepancy is when the gravity wave becomes the dominant forcing mechanism. Gravity waves are generated on the coast and radiate to far distances. While the nearshore rainfall migration is mainly determined by land breeze, gravity waves appear to dominate farther offshore.
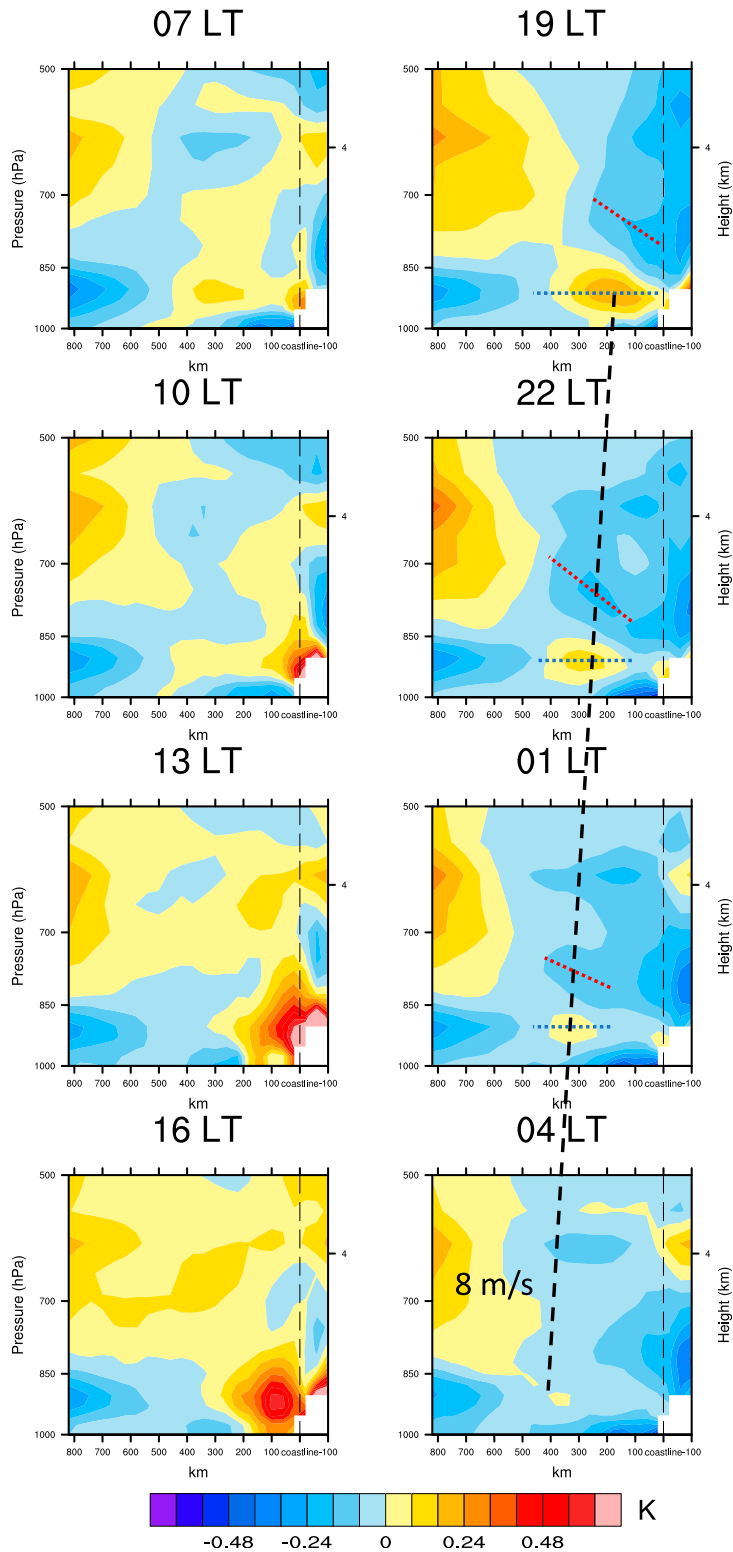
FIG. 13. Cross sections of the ERA5 temperature anomalies averaged along the narrow dimension of the gray-outlined box in Fig. 1 for all offshore rain events. The thick black dashed line marks the propagation of a low-level warm anomaly, which has a speed of $8 \, \mathrm{m \, s^{-1}}$. The apparent slope of the phase lines is indicated with blue (red) dotted lines.

5. Summary

This study focuses on the characteristics of nocturnal rainfall events that propagate offshore from Padang on the west coast of Sumatra using BMKG C-band radar observations and ERA5 reanalysis fields. Nocturnal offshore rainfall has been discussed by many previous papers through both observations and modeling, but this is the first study analyzing offshore rainfall event by event and demonstrating event frequency in terms of the MJO and season. The two major possible drivers for the offshore rainfall propagation events are also discussed in detail.

A total of 280 days of BMKG radar data at Padang was obtained during 2018. Using daily Hovmöllers and rain-map movies, 117 nocturnal offshore rainfall events were identified. On average, nocturnal offshore rainfall starts near the coast at around 1800 LT and propagates seaward with a mean speed of $4.5 \, \text{m s}^{-1}$ within 180 km offshore of Padang. Along a 200-km-long section of the coastline of Sumatra, approximately 40% of the days see offshore rainfall migration. The local diurnal cycle over the MC interacts strongly with the passage of the MJO. Based on both the classic multivariate MJO RMM index and a revised RMM index that more heavily weights convection, it was found that most offshore events occur during MJO phases 1–3 (when the MJO is active over the Indian Ocean and low-level winds are transitioning from weak offshore easterlies to moderate onshore westerlies as the MJO approaches Sumatra) and when the MJO is inactive, and the least events occur in phases 4–6 (when the MJO is active over the MC and the west Pacific and strong low-level westerlies are affecting Sumatra). The large number of offshore events that occur in phases 1–3 implies that offshore-propagating systems play a significant role in rainfall off the west coast of Sumatra as the MJO approaches the MC. The occurrence of offshore rainfall also varies seasonally due to changes of circulation by the Asian-Australian monsoon, with more events occurring during the (rainier) transition seasons and less events occurring when monsoons are active to the north and south of Sumatra, producing stronger low-level westerly winds over West Sumatra, especially during DJF. The propagation speed of the offshore rainfall is found to vary by season, with the fastest speeds in JJA when background coast-normal winds are weakest. When separated into convective and stratiform rain, stratiform rain is found to propagate seaward at $6 \, \text{m s}^{-1}$, faster than the $4.5 \, \text{m s}^{-1}$ speed of convective rain, presumably because of the upper-level easterly (offshore) winds increasing the speed of the stratiform cloud deck relative to the low-level westerly (onshore) winds.

We consider the land breeze and other impacts from gravity waves separately in this study in terms of forcing mechanisms for the offshore rainfall propagation. Low-level convergence formed between the offshore land breeze and onshore background wind propagates offshore in the early evening at a speed of $5.5 \, \text{m s}^{-1}$. Low-level convergence propagation is slightly faster than the speed of the convective rain, but is a better match than gravity waves. Gravity wave signals were analyzed using vertical cross sections of the diurnal temperature anomalies with distance from the coast. A low-level warm anomaly was found to propagate offshore at a speed of $8 \, \text{m s}^{-1}$ in the evening to early morning, and a cold anomaly with a different apparent phase slope is found above the warm anomaly. In its broad features, the disturbance appears to resemble the response to a pulsed or rapid-onset heat source, perhaps reflecting the relatively rapid formation of convection over the coastal topography in the late morning/early afternoon. From the depth scale of the disturbance, the linear propagation speed of the wave is estimated to be roughly 6.5–$8.5 \, \text{m s}^{-1}$, consistent with the observed value of $8 \, \text{m s}^{-1}$. The warm anomaly destabilizes the lower atmosphere ahead of offshore rainfall.

Therefore, we propose that the land breeze is the main driver of offshore rainfall near the coast of West Sumatra, while gravity waves play a secondary role by modulating the environment to be more conducive to convection. Previous studies have also shown that the late evening to early morning precipitation maximum over the coastal ocean reaches as far as many hundreds of kilometers and propagates faster farther offshore, therefore, farther offshore beyond our radar domain, gravity waves may dominate. However, a more definitive conclusion needs to be drawn with further quantitative analysis such as determining the amount of rainfall produced by each of the mechanisms, likely through modeling work. Besides the two mechanisms discussed in this paper, there are other factors that may also play a role in the offshore rainfall propagation but are beyond the scope of this study. For example, Wu et al. (2009) showed from model simulations that cold surface outflow from convection reduces offshore convective inhibition. Jain et al. (2018) reported from high-resolution simulations that saturated downdrafts from mesoscale convective systems can generate a horizontal momentum tendency to boost the rainfall propagation. We plan to address variations in the forcing mechanism and associated structure of the gravity wave response in future modeling and theory work.

Data availability statement. All ERA5 fields analyzed in this study are openly available from the Copernicus Climate Change Service (C3S) Climate Data Store (https://cds.climate.copernicus.eu/). The gridded rain maps and convective–stratiform classifications derived from the BMKG Padang C-band radar observations will be archived at the Texas A&M University OAKTrust Digital Repository (http://oaktrust.library.tamu.edu). The processed rain and wind data from the Padang surface station are available by request from G. Deranadyan (gumilangderanadyan@yahoo.com) at BMKG.

REFERENCES

Aves, S. L., and R. H. Johnson, 2008: The diurnal cycle of convection over the northern South China Sea. *J. Meteor. Soc. Japan*, **86**, 919–934, https://doi.org/10.2151/jmsj.86.919.

Belmonte Rivas, M., and A. Stoffelen, 2019: Characterizing ERA-Interim and ERA5 surface wind biases using ASCAT. *Ocean Sci.*, **15**, 831–852, https://doi.org/10.5194/os-15-831-2019.

Benjamin, T. B., 1968: Gravity currents and related phenomena. *J. Fluid Mech.*, **31**, 209–248, https://doi.org/10.1017/S0022112068000133.

Biasutti, M., S. E. Yuter, S. D. Burleyson, and A. H. Sobel, 2012: Very high resolution rainfall patterns measured by TRMM precipitation radar: Seasonal and diurnal cycles. *Climate Dyn.*, **39**, 239–258, https://doi.org/10.1007/s00382-011-1146-6.

Birch, C. E., S. Webster, S. C. Peatman, D. J. Parker, A. J. Matthews, Y. Li, and M. E. E. Hassim, 2016: Scale interactions between the MJO and the western Maritime Continent. *J. Climate*, **29**, 2471–2492, https://doi.org/10.1175/JCLI-D-15-0557.1.

Coppin, D., and G. Bellon, 2019: Physical mechanisms controlling the offshore propagation of convection in the tropics: 1. Flat Island. *J. Adv. Model. Earth Syst.*, **11**, 3251–3264, https://doi.org/10.1029/2019MS001793.

Dickinson, R. E., 1969: Propagators of atmospheric motions: 1. Excitation by point impulses. *Rev. Geophys.*, **7**, 483–514, https://doi.org/10.1029/RG007i003p00483.

Du, Y., and R. Rotunno, 2018: Diurnal cycle of rainfall and winds near the south coast of China. *J. Atmos. Sci.*, **75**, 2065–2082, https://doi.org/10.1175/JAS-D-17-0397.1.

——, ——, and F. Zhang, 2019: Impact of vertical wind shear on gravity wave propagation 3 in the land–sea breeze circulation at the equator. *J. Atmos. Sci.*, **76**, 3247–3265, https://doi.org/10.1175/JAS-D-19-0069.1.

Gille, S. T., S. G. Llewellyn Smith, and N. M. Statom, 2005: Global observations of the land breeze. *Geophys. Res. Lett.*, **32**, L05605, https://doi.org/10.1029/2004GL022139.

Gray, W. M., and R. W. Jacobson, 1977: Diurnal variation of deep cumulus convection. *Mon. Wea. Rev.*, **105**, 1171–1188, https://doi.org/10.1175/1520-0493(1977)105<1171:DVODCC>2.0.CO;2.

Hassim, M. E. E., T. P. Lane, and W. W. Grabowski, 2016: The diurnal cycle of rainfall over New Guinea in convection-permitting WRF simulations. *Atmos. Chem. Phys.*, **16**, 161–175, https://doi.org/10.5194/acp-16-161-2016.

Hersbach, H., and Coauthors, 2020: The ERA5 global reanalysis. *Quart. J. Roy. Meteor. Soc.*, **146**, 1999–2049, https://doi.org/10.1002/qj.3803.

Houze, R. A., Jr., 1997: Stratiform precipitation in regions of convection: A meteorological paradox? *Bull. Amer. Meteor. Soc.*, **78**, 2179–2196, https://doi.org/10.1175/1520-0477(1997)078<2179:SPIROC>2.0.CO;2.

——, S. G. Geotis, F. D. Marks Jr, and A. K. West, 1981: Winter monsoon convection in the vicinity of North Borneo. Part I: Structure and time variation of the clouds and precipitation. *Mon. Wea. Rev.*, **109**, 1595–1614, https://doi.org/10.1175/1520-0493(1981)109<1595:WMCITV>2.0.CO;2.

Ichikawa, H., and T. Yasunari, 2006: Time–space characteristics of diurnal rainfall over Borneo and surrounding oceans as observed by TRMM-PR. *J. Climate*, **19**, 1238–1260, https://doi.org/10.1175/JCLI3714.1.

——, and ——, 2007: Propagating diurnal disturbances embedded in the Madden–Julian Oscillation. *Geophys. Res. Lett.*, **34**, L18811, https://doi.org/10.1029/2007GL030480.

Jain, D., A. Chakraborty, and R. S. Nanjundaiah, 2018: A mechanism for the southward propagation of mesoscale convective systems over the Bay of Bengal. *J. Geophys. Res. Atmos.*, **123**, 3893–3913, https://doi.org/10.1002/2017JD027470.

Kikuchi, K., and B. Wang, 2008: Diurnal precipitation regimes in the global tropics. *J. Climate*, **21**, 2680–2696, https://doi.org/10.1175/2007JCLI2051.1.

Li, Y. P., and R. E. Carbone, 2015: Offshore propagation of coastal precipitation. *J. Atmos. Sci.*, **72**, 4553–4568, https://doi.org/10.1175/JAS-D-15-0104.1.

Liu, P., and Coauthors, 2016: A revised real-time multivariate MJO index. *Mon. Wea. Rev.*, **144**, 627–642, https://doi.org/10.1175/MWR-D-15-0237.1.

Long, C. N., and Coauthors, 2011: ARM MJO investigation experiment on Gan Island (AMIE-Gan) science plan. DOE/ARM Tech. Rep. DOE/SC-ARM-11-005, 63 pp.

Love, B. S., A. J. Matthews, and G. M. Lister, 2011: The diurnal cycle of precipitation over the Maritime Continent in a high-resolution atmospheric model. *Quart. J. Roy. Meteor. Soc.*, **137**, 934–947, https://doi.org/10.1002/qj.809.

Madden, R. A., and P. R. Julian, 1972: Description of global-scale circulation cells in the tropics with a 40–50 day period. *J. Atmos. Sci.*, **29**, 1109–1123, https://doi.org/10.1175/1520-0469(1972)029<1109:DOGSCC>2.0.CO;2.

Mapes, B. E., 1993: Gregarious tropical convection. *J. Atmos. Sci.*, **50**, 2026–2037, https://doi.org/10.1175/1520-0469(1993)050<2026:GTC>2.0.CO;2.

——, T. T. Warner, and M. Xu, 2003: Diurnal patterns of rainfall in northwestern South America. Part III: Diurnal gravity waves and nocturnal convection offshore. *Mon. Wea. Rev.*, **131**, 830–844, https://doi.org/10.1175/1520-0493(2003)131<0830:DPORIN>2.0.CO;2.

Mori, S., and Coauthors, 2004: Diurnal land–sea rainfall peak migration over Sumatera Island, Indonesian Maritime Continent, observed by TRMM satellite and intensive rawinsonde soundings. *Mon. Wea. Rev.*, **132**, 2021–2039, https://doi.org/10.1175/1520-0493(2004)132<2021:DLRPMO>2.0.CO;2.

——, and Coauthors, 2011: Convective systems developed along the coastline of Sumatera Island, Indonesia, observed with an X-band Doppler radar during the HARIMAU2006 campaign. *J. Meteor. Soc. Japan*, **89A**, 61–81, https://doi.org/10.2151/jmsj.2011-A04.

Ohsawa, T., H. Ueda, T. Hayashi, A. Watanabe, and J. Matsumoto, 2001: Diurnal variations of convective activity and rainfall in tropical Asia. *J. Meteor. Soc. Japan*, **79**, 333–352, https://doi.org/10.2151/jmsj.79.333.

Park, M. S., C. H. Ho, J. Kim, and R. L. Elsberry, 2011: Diurnal circulations and their multi-scale interaction leading to rainfall over the South China Sea upstream of the Philippines during intraseasonal monsoon westerly wind bursts. *Climate Dyn.*, **37**, 1483–1499, https://doi.org/10.1007/s00382-010-0922-z.

Parker, M. D., and R. H. Johnson, 2000: Organizational modes of midlatitude mesoscale convective systems. *Mon. Wea. Rev.*, **128**, 3413–3436, https://doi.org/10.1175/1520-0493(2001)129<3413:OMOMMC>2.0.CO;2.

Peatman, S. C., A. J. Matthews, and D. P. Stevens, 2014: Propagation of the Madden–Julian Oscillation through the Maritime Continent and scale interaction with the diurnal cycle of precipitation. *Quart. J. Roy. Meteor. Soc.*, **140**, 814–825, https://doi.org/10.1002/qj.2161.

Qian, T., C. C. Epifanio, and F. Zhang, 2009: Linear theory calculations for the sea breeze in a background wind: The equatorial case. *J. Atmos. Sci.*, **66**, 1749–1763, https://doi.org/10.1175/2008JAS2851.1.

——, ——, and ——, 2012: Topographic effects on the tropical land and sea breeze. *J. Atmos. Sci.*, **69**, 130–149, https://doi.org/10.1175/JAS-D-11-011.1.

Ramon, J., L. Lledó, V. Torralba, A. Soret, and F. J. Doblas-Reyes, 2019: What global reanalysis best represents near-surface winds? *Quart. J. Roy. Meteor. Soc.*, **145**, 3236–3251, https://doi.org/10.1002/qj.3616.

Rauniyar, S. P., and K. J. E. Walsh, 2011: Scale interaction of the diurnal cycle of rainfall over the Maritime Continent and Australia: Influence of the MJO. *J. Climate*, **24**, 325–348, https://doi.org/10.1175/2010JCLI3673.1.

Rotunno, R., 1983: On the linear theory of the land and sea breeze. *J. Atmos. Sci.*, **40**, 1999–2009, https://doi.org/10.1175/1520-0469(1983)040<1999:OTLTOT>2.0.CO;2.

Ruppert, J. H., and F. Q. Zhang, 2019: Diurnal forcing and phase locking of gravity waves in the Maritime Continent. *J. Atmos. Sci.*, **76**, 2815–2835, https://doi.org/10.1175/JAS-D-19-0061.1.

——, X. Chen, and F. Zhang, 2020: Convectively forced diurnal gravity waves in the Maritime Continent. *J. Atmos. Sci.*, **77**, 1119–1136, https://doi.org/10.1175/JAS-D-19-0236.1.

Seitter, K. L., 1986: A numerical study of atmospheric density current motion including the effects of condensation. *J. Atmos. Sci.*, **43**, 3068–3076, https://doi.org/10.1175/1520-0469(1986)043<3068:ANSOAD>2.0.CO;2.

Short, E., C. L. Vincent, and T. P. Lane, 2019: Diurnal cycle of surface winds in the Maritime Continent observed through satellite scatterometry. *Mon. Wea. Rev.*, **147**, 2023–2044, https://doi.org/10.1175/MWR-D-18-0433.1.

Simpson, J. E., and R. E. Britter, 1980: A laboratory model of an atmospheric mesofront. *Quart. J. Roy. Meteor. Soc.*, **106**, 485–500, https://doi.org/10.1002/qj.49710644907.

Sobel, A. H., C. D. Burleyson, and S. E. Yuter, 2011: Rain on small tropical islands. *J. Geophys. Res.*, **116**, D08102, https://doi.org/10.1029/2010JD014695.

Steiner, M., R. A. Houze Jr., and S. E. Yuter, 1995: Climatological characterization of three-dimensional storm structure from operational radar and rain gauge data. *J. Appl. Meteor.*, **34**, 1978–2007, https://doi.org/10.1175/1520-0450(1995)034<1978:CCOTDS>2.0.CO;2.

Tian, B. J., D. E. Waliser, and E. J. Fetzer, 2006: Modulation of the diurnal cycle of tropical deep convective clouds by the MJO. *Geophys. Res. Lett.*, **33**, L20704, https://doi.org/10.1029/2006GL027752.

Vincent, C. L., and T. P. Lane, 2016: Evolution of the diurnal precipitation cycle with the passage of a Madden–Julian oscillation event through the Maritime Continent. *Mon. Wea. Rev.*, **144**, 1983–2005, https://doi.org/10.1175/MWR-D-15-0326.1.

Wakimoto, R. M., 1982: The life cycle of thunderstorm gust fronts as viewed with Doppler radar and rawinsonde data.

Mon. Wea. Rev., **110**, 1060–1082, https://doi.org/10.1175/1520-0493(1982)110<1060:TLCOTG>2.0.CO;2.

Wang, S., and A. H. Sobel, 2017: Factors controlling rain on small tropical islands: Diurnal cycle, large-scale wind speed, and topography. *J. Atmos. Sci.*, **74**, 3515–3532, https://doi.org/10.1175/JAS-D-16-0344.1.

Warner, T. T., B. E. Mapes, and M. Xu, 2003: Diurnal patterns of rainfall in northwestern South America. Part II: Model simulations. *Mon. Wea. Rev.*, **131**, 813–829, https://doi.org/10.1175/1520-0493(2003)131<0813:DPORIN>2.0.CO;2.

Wheeler, M. C., and H. H. Hendon, 2004: An all-season real-time multivariate MJO index: Development of an index for monitoring and prediction. *Mon. Wea. Rev.*, **132**, 1917–1932, https://doi.org/10.1175/1520-0493(2004)132<1917:AARMMI>2.0.CO;2.

Wu, P. M., M. D. Yamanaka, and J. Matsumoto, 2008: The formation of nocturnal rainfall offshore from convection over western Kalimantan (Borneo) Island. *J. Meteor. Soc. Japan*, **86A**, 187–203, https://doi.org/10.2151/jmsj.86A.187.

——, M. Hara, J. Hamada, M. D. Yamanaka, and F. Kimura, 2009: Why a large amount of rain falls over the sea in the vicinity of western Sumatra Island during nighttime. *J. Appl. Meteor. Climatol.*, **48**, 1345–1361, https://doi.org/10.1175/2009JAMC2052.1.

Yang, G. Y., and J. Slingo, 2001: The diurnal cycle in the tropics. *Mon. Wea. Rev.*, **129**, 784–801, https://doi.org/10.1175/1520-0493(2001)129<0784:TDCITT>2.0.CO;2.

Yokoi, S., and Coauthors, 2017: Diurnal cycle of precipitation observed in the western coastal area of Sumatra Island: Offshore preconditioning by gravity waves. *Mon. Wea. Rev.*, **145**, 3745–3761, https://doi.org/10.1175/MWR-D-16-0468.1.

——, S. Mori, F. Syamsudin, U. Haryoko, and B. Geng, 2019: Environmental conditions for nighttime offshore migration of precipitation area as revealed by in situ observation off Sumatra Island. *Mon. Wea. Rev.*, **147**, 3391–3407, https://doi.org/10.1175/MWR-D-18-0412.1.

Yoneyama, K., C. D. Zhang, and C. N. Long, 2013: Tracking pulses of the Madden–Julian oscillation. *Bull. Amer. Meteor. Soc.*, **94**, 1871–1891, https://doi.org/10.1175/BAMS-D-12-00157.1.

Zhang, C. D., and J. Ling, 2017: Barrier effect of the Indo-Pacific Maritime Continent on the MJO: Perspectives from tracking MJO precipitation. *J. Climate*, **30**, 3439–3459, https://doi.org/10.1175/JCLI-D-16-0614.1.

Zhou, L., and Y. Q. Wang, 2006: Tropical Rainfall Measuring Mission observation and regional model study of precipitation diurnal cycle in the New Guinean region. *J. Geophys. Res.*, **111**, D17104, https://doi.org/10.1029/2006JD007243.